Automated high-resolution satellite-derived coastal bathymetry mapping

Matthew J. McCarthy [a,b,*], Daniel B. Otis [b], David Hughes [a], Frank E. Muller-Karger [b]

[a] Oak Ridge National Laboratory, Geospatial Science and Human Security Division, Remote Sensing Group, 1 Bethel Valley Road, Oak Ridge, TN 37830, USA
[b] Institute for Marine Remote Sensing, College of Marine Science, University of South Florida, 140 7th Ave. South, Saint Petersburg, FL 33701, USA

A R T I C L E   I N F O

A B S T R A C T

Accurate and up-to-date maps of coastal bathymetry are fundamental for coastal resource management, commercial and military navigation, and aquaculture, among many applications. Existing methods for bathymetry mapping require intensive and costly field surveys or targeted aerial captures, neither of which are easily or affordably replicated for repeat mapping and change monitoring. Satellite-derived bathymetry (SDB), however, offers the potential to map shallow water bodies repeatedly and efficiently with high spatial and temporal resolution (i.e., daily-weekly at 5 m or better). One challenge to large-scale implementation of SDB lies in the automated derivation of inherent water column properties such that they may be accurately compensated for across a variety of depth and substrate conditions. Here we present an algorithm that leverages WorldView (Maxar/Digital Globe[TM]) satellite imagery to map the entire 3700 km[2] Florida Keys (USA) island chain at 2-meter resolution without the need for any in-situ data collections. Preprocessing included radiometric calibration, atmospheric correction, automated deglinting, and automated detection of optically deep water, which was then used to estimate chlorophyll-a concentration assuming that the study area is primarily comprised of Case-I water (i.e., those where the optical signal is dominated by water, Chlorophyll-a in phytoplankton, and properties that vary in proportion to Chlorophyll-a concentration). Estimating Chlorophyll-a concentration allowed us to calculate the appropriate tuning coefficients used in a spectral band ratio equation for estimating bathymetry. The entire process was fully automated from ingestion of Level-1B image to bathymetry raster output. Mapping the Florida Keys from Key Largo to Key West required 34 WorldView images and was completed in approximately 27 min for an average processing time of 47 s per image using a single GPU core (i.e., supercomputing resources were not needed). After combining the products (mosaicking) in ArcMap, the wall-to-wall bathymetry map was validated against a LiDAR-derived bathymetry model with over 600,000 points; results show an RMSE of 1.95 m over depths from 0 to 15 m.

1. Introduction

Accurate and up-to-date maps of coastal bathymetry are critical for multiple sectors and applications, from vessel navigation to port construction, coastal resource management and urban planning amid accelerating sea-level rise (Mayer et al., 2018; Stocker et al., 2013). Traditional approaches to mapping bathymetry rely on ship soundings or LiDAR measurements from aerial vehicles that are costly, labor-intensive, and time-consuming (Li et al., 2019; Stumpf et al., 2003). As a result, approximately 70–80% of the global coastal zone lacks accurate bathymetry maps, let alone those of high spatio-temporal resolution (Caballero and Stumpf, 2020; Mayer et al., 2018).

Satellite-derived bathymetry (SDB) has existed in practice since at least the 1970s to estimate water depth in clear, shallow water. The process is based on the observation of water-leaving radiance, knowledge of light attenuation with depth in clear water, and a model calibrated using in-situ depth measurements (Stumpf et al., 2003). More complex approaches use radiative transfer modeling of the water body's inherent optical properties (IOPs) (Hedley et al., 2005; Hughes et al., 2001; Kutser et al., 2020; Sandidge and Holyer, 1998). The remote sensing of aquatic properties includes many challenges, such as detecting and correcting for sun glint, wave action, high suspended sediment, or type of bottom (Kay et al., 2009; Martin et al., 2016).

Many SDB efforts choose water bodies that are Case 1 (i.e., phytoplankton-dominated) such that Chlorophyll-a (Chl-a) is the primary driver of light attenuation because the effect of phytoplankton on

light attenuation is relatively well-constrained by decades of ocean color research. Therefore, recent SDB methods have focused on accounting for attenuation due to Chl-a concentration in an image using empirical relationships (Li et al., 2019; Ma et al., 2021), assumptions about the concentration (Kerr and Purkis, 2018), or by selecting "clean-water" images with negligible turbidity (Li et al., 2021). With the Chl-a concentration for each image measured or assumed, a band-ratio approach is then applied using coefficients tuned to account for Chlorophyll-induced attenuation. However, "clean-water" images do not always exist, arbitrary Chl-a concentration assumptions can produce substantial errors, and confounding factors such as sunglint can preclude accurate estimates of Chl-a concentration from the spectral data. We developed an algorithm that fully automates the preprocessing, deglinting (as needed), Chl-a concentration estimation, and bathymetry mapping of 2-meter resolution satellite imagery.

Recent advances in image processing and high-performance computing have paved the way for efficient processing of large volumes of imagery and other data (McCarthy et al., 2018; Shelestov et al., 2017). Simultaneous advances in site-independent SDB algorithms, including forward physical-modeling of light attenuation with depth, and adaptive bathymetry estimation, no longer require field calibration (Kerr and Purkis, 2018; Li et al., 2019). In this study, we derived and applied site-agnostic algorithms to map 34 satellite images covering the Florida Keys from Key Largo to Key West (183 km) in a fully automated protocol.

2. Materials and methods

2.1. Study area

We applied our automated algorithm to the Florida Keys, USA (Fig. 1), which spans ~183 km in length. We selected an area of 3700 km^2 for mapping a target bathymetry range of 0–15 m over diverse benthic substrates (e.g. sand, coral, seagrasses, hard bottom). Much of the area has relatively clear "Case 1" waters (i.e., water column constituents are phytoplankton and co-varying variables), and was mapped with LiDAR in the wake of Hurricane Irma (*NOAA Hurricane Irma, Florida Keys: Supplemental LiDAR & Shoreline Mapping*, 2020). We matched the area covered by the LiDAR bathymetry map between Key Largo and Key West for comparison with our satellite-derived bathymetry products.

2.2. WorldView imagery

We used 34 WorldView (WV) images collected by the WorldView-2 (WV2) and WorldView-3 (WV3) satellite sensors owned and operated by Maxar/Digital Globe™ (Table 1). WV2 and WV3 were launched in 2009 and 2014, respectively, as polar-orbiting, push-broom multispectral sensors that record data in eight channels spanning the visible to near-infrared spectral range (WV3 offers additional wavelengths not included in this study) with spatial resolution in the 1-2-meter range depending on viewing angle. Images were ordered in Level-1B format as GeoTIFFs.
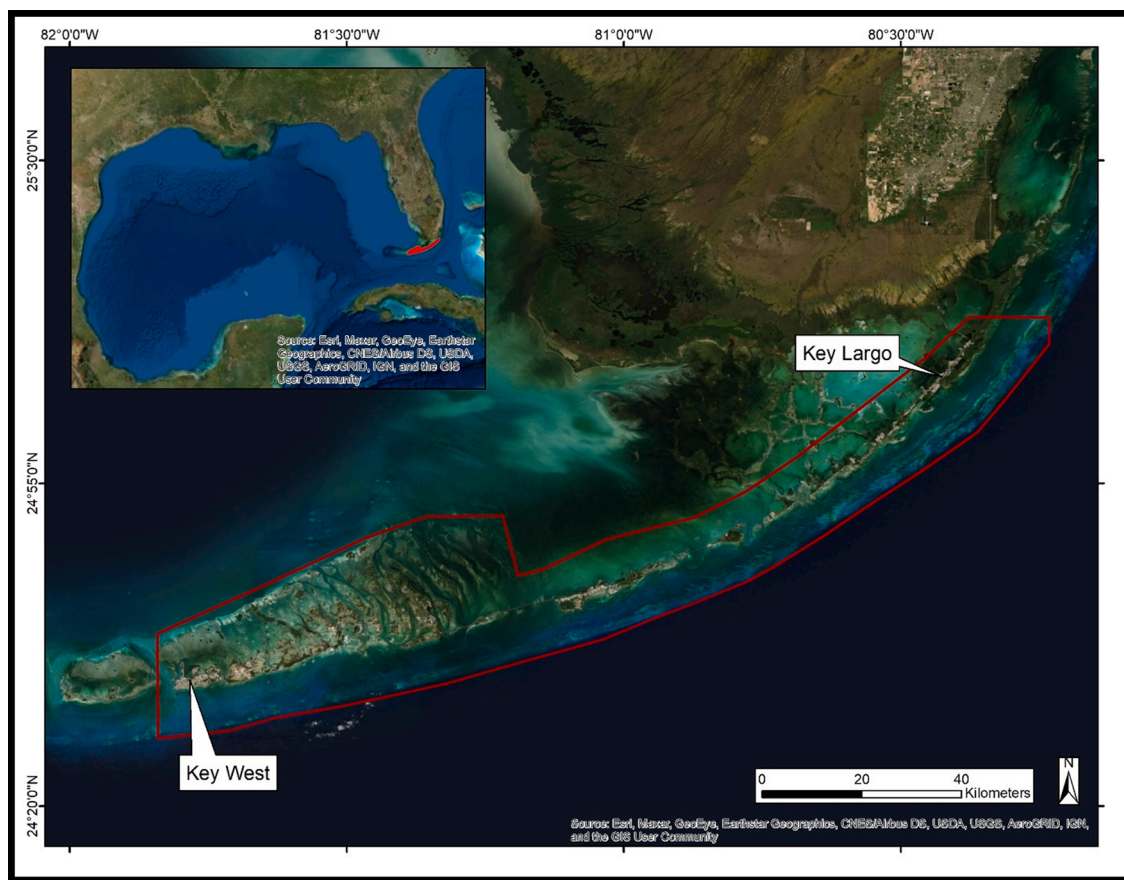

Fig. 1. The Florida Keys study area. The map was restricted to the region bounded in red to coincide with the extent of LiDAR data and available WorldView satellite imagery (Imagery is from ArcGIS "Imagery" basemap). (For interpretation of the references to color in this figure legend, the reader is referred to the web version of this article.)

Table 1
Image name, location, and date for satellite imagery used.

| Filename	Lat (UL)	Lat (LR)	Lon (UL)	Lon (LR)	Year	Month	Day
10AUG13161421-M1BS-013431031010	25.11683	24.96801	−80.4575	−80.2885	2010	8	13
12NOV19163316-M1BS-500064643130	24.66029	24.52404	−81.8459	−81.6838	2012	11	19
12NOV19163317-M1BS-500064643130	24.55014	24.43911	−81.8458	−81.6838	2012	11	19
15APR18160013-M1BS-013455264010	24.79311	24.69694	−81.504	−81.3491	2015	4	18
15APR18160014-M1BS-013455264010	24.72845	24.63232	−81.5038	−81.3493	2015	4	18
15APR18160015-M1BS-013455264010	24.66385	24.59085	−81.5036	−81.3494	2015	4	18
15APR18160025-M1BS-013442579010	24.67771	24.58895	−81.3653	−81.2162	2015	4	18
15APR18160026-M1BS-013442579010	24.74106	24.64123	−81.3653	−81.2162	2015	4	18
15APR18160028-M1BS-013442579010	24.86829	24.76559	−81.3654	−81.2161	2015	4	18
15APR18160100-M1BS-013442580010	24.7481	24.62952	−81.2334	−81.08	2015	4	18
15APR18160101-M1BS-013442580010	24.68356	24.56978	−81.2332	−81.0802	2015	4	18
15APR24155535-M1BS-013442582010	24.80838	24.69489	−81.1017	−80.9302	2015	4	24
15APR24155536-M1BS-013442582010	24.74368	24.63041	−81.1015	−80.9304	2015	4	24
15APR24155537-M1BS-013442582010	24.67905	24.56788	−81.1012	−80.9306	2015	4	24
15NOV12161727-M1BS-013442583010	25.15469	25.0018	−80.5146	−80.3206	2015	11	12
16JAN16162157-M1BS-013442581010	24.69494	24.59645	−81.6951	−81.5602	2016	1	16
16JAN16162158-M1BS-013442581010	24.63002	24.53146	−81.695	−81.5602	2016	1	16
17FEB15160921-M1BS-013442584010	24.72282	24.58756	−80.8991	−80.7355	2017	2	15
17FEB15160923-M1BS-013442584010	24.83317	24.68696	−80.8992	−80.7356	2017	2	15
17OCT19162454-M1BS-013199222010	24.83919	24.7422	−80.9713	−80.8332	2017	9	19
17OCT19162509-M1BS-013199223010	24.69588	24.59331	−81.0893	−80.953	2017	9	19
17OCT19162539-M1BS-013199221010	24.83692	24.72405	−81.3384	−81.1915	2017	9	19
17OCT19162555-M1BS-013199224010	24.76347	24.64781	−81.4713	−81.3158	2017	9	19
17OCT19162556-M1BS-013199224010	24.82932	24.71104	−81.4721	−81.3151	2017	9	19
18AUG22162606-M1BS-013442587010	25.21654	25.11778	−80.3729	−80.2305	2018	8	22
18AUG22162607-M1BS-013442587010	25.15188	25.05334	−80.3729	−80.2306	2018	8	22
18AUG22162608-M1BS-013442587010	25.08727	24.98899	−80.3728	−80.2306	2018	8	22
18FEB16162712-M1BS-013442578010	24.99815	24.97844	−80.6663	−80.4573	2018	2	16
18NOV10161106-M1BS-013442588010	25.01037	24.8762	−80.6638	−80.4962	2018	11	10
18NOV10161107-M1BS-013442588010	24.91082	24.76616	−80.6637	−80.4964	2018	11	10
18NOV10161120-M1BS-013442589010	24.83467	24.68783	−80.8138	−80.6468	2018	11	10
18NOV10161121-M1BS-013442589010	24.94515	24.79716	−80.8139	−80.6467	2018	11	10
18NOV10161216-M1BS-013442586010	24.70899	24.56988	−81.6048	−81.4157	2018	11	10
19APR28155605-M1BS-013442590010	25.0306	24.87505	−80.5873	−80.3639	2019	4	28
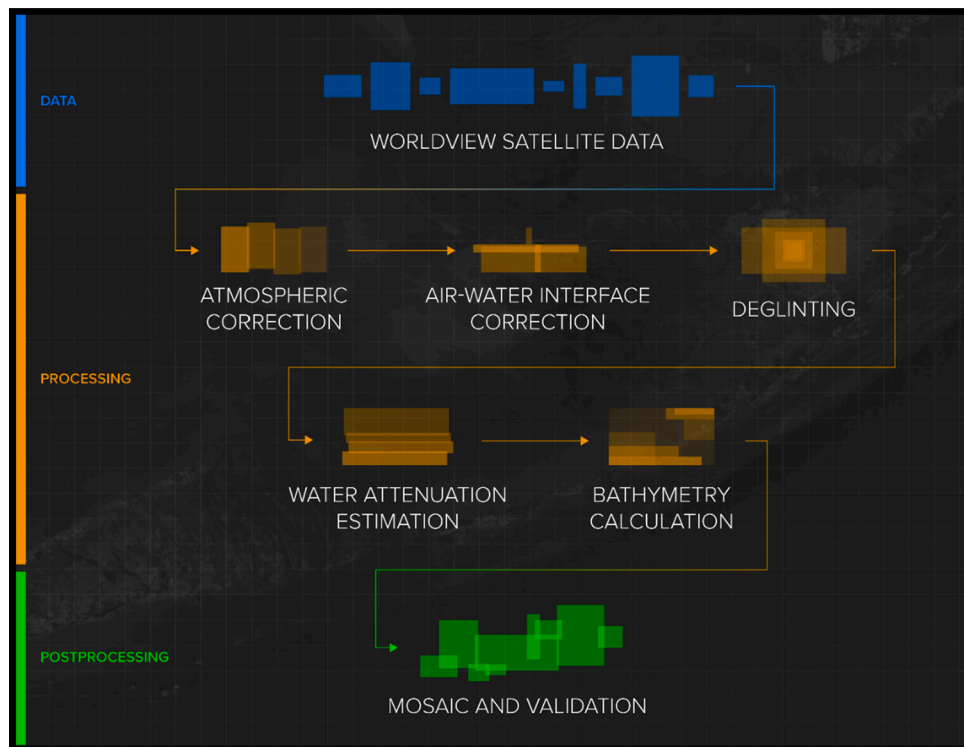
Fig. 2. Automated bathymetry mapping pipeline.

2.3. Image preprocessing

Image processing followed the pipeline shown in Fig. 2 to standardize all images for accurate comparative analysis. Preprocessing included transforming digital number to at-sensor radiances using the calibration factors supplied with each image's metadata. Further processing followed the atmospheric- and air-water-interface-correction protocol of Kerr and Perkis (2018 equations 2–6 and references therein), which account for date, time, Earth-Sun distance, latitude, longitude, and Sun and satellite geometries. Rayleigh path radiance was calculated using the protocol of Dash et al. (2012 and references therein). The output generated was subsurface remote sensing reflectance (r_{rs}).

2.4. Deglinting

Sun glint is a common problem in aquatic satellite images caused by the specular reflection of sunlight on the surface of the water, which often saturates a sensor. Glinted pixels must either be corrected or discarded from further processing. Correcting for sun glint in high-resolution images can be done in a variety of ways (Hochberg et al., 2003; Kay et al., 2009), but typically requires manual identification of glinted samples, which precludes automation. To incorporate glint correction into our automated protocol we first predicted the likelihood of glint presence in the scene. Sun glint depends on the sun-target-sensor geometry, and is most likely to occur when sun and sensor azimuths are approximately 180 degrees apart, and with higher zenith angles (Jackson and Alpers, 2010; Zhou et al., 2017). To predict glint likelihood, we derived the following equations to quantify relative sun and sensor azimuth and zenith angles, normalized to their maximum likely values:

$$AZ_{rel} = (|AZ_{sun} - AZ_{sat} - 180|)/180 \qquad (1)$$

$$ZN_{rel} = (ZN_{sun} + ZN_{sat})/120 \qquad (2)$$

where AZ refers to azimuth angles, and ZN refers to zenith angles. By summing AZ_{rel} and ZN_{rel} we would conservatively predict that sun glint is likely for values less than or equal to 0.65. This threshold was determined by manually evaluating an ancillary dataset containing glinted and glint-free images.

If the scene was likely to contain sun glint, glint correction was performed as described in McCarthy et al. (2020) to automatically identify the glinted-pixel spectral profile and correct it for every glinted image prior to bathymetry estimation.

2.5. Bathymetry algorithm

Bathymetry was calculated with the Stumpf et al. (2003) band ratio method as

$$z = B1 \frac{\ln(Mr_{rs,i})}{\ln(Mr_{rs,j})} + B0 \qquad (3)$$

where i and j correspond to the blue and green bands, respectively, M is a scaling factor of 1000, and B1 and B0 are tuning coefficients. This model is based on the exponential attenuation of light with depth, the rate of which varies with wavelength and water-column optical properties. The tuning coefficients, B1 and B0, were derived by Stumpf et al. (2003) through linear regression of a band ratio from a single satellite image against observed depths from 0 to 12 m. Kerr and Perkis (2018) developed a forward-modeled algorithm to estimate the coefficients for multiple satellite sensors in different study areas with specific benthic substrate types and assuming a Chl-a concentration of 0.2 mg m^{-3}. Li et al. (2019) developed an adaptive bathymetry estimation algorithm that relies on the assumptions that (1) optically deep water in an image can be used to estimate the inherent and apparent water column properties, and (2) that the relatively small coverage of a single image comprises similar attenuation conditions throughout.

Our approach is to further automate the Li et al. (2019) method by automatically identifying optically deep water, using it to estimate the image's attenuation properties (i.e. Chl-a), and calculating the tuning coefficients from a revised version of the Li et al. (2019) Eqs. (10) and (11).

Water was identified as pixels with a reflectance value < 0.2 in the NIR1 band (i.e., band 7). Optically deep water (ODW) was defined as water pixels containing NIR1 values within the 5th to 10th percentile of all water pixels. This range was selected based on Overstreet and Legleiter (2017), and the observation that the darkest NIR1 pixels (i.e. 0-5th percentile) were anomalous dark bodies (e.g. cloud shadow or dark freshwater bodies) that did not represent the coastal-water attenuation properties targeted for this work.

Chlorophyll-a concentration (Chl_a) was estimated based on:

$$w = r_{rs}(Green) - 0.46*r_{rs}(Red) - 0.54*r_{rs}(Coastal) \qquad (4)$$

$$Chl_a = 10^{(-0.4909 + 191.659*w)} \qquad (5)$$

where w was calculated for every ODW pixel before taking the median of those w values less than 0 (Hu et al., 2012; Werdell and Bailey, 2005). We replaced the Blue band with the Coastal band in Eq. (4) because the original equation by Hu et al. (2012) used wavelength 443 nm, which is closer to the center wavelength of the Coastal Band, and following the Kerr and Perkis (2018) finding that, in Case 1 waters, the Coastal band has a lower attenuation rate than the Blue band. Tuning coefficients were calculated as:

$$B1 = 52.083*e^{(1.77*Chla)} \qquad (6)$$

$$B0 = 50.156*e^{(1.70*Chla)} \qquad (7)$$

The exponential scalars from Li et al. (2019) were established for the Planet Dove satellites, so we calculated ours by setting B1 and B0 equal to the field-based values calculated by Kerr and Perkis (2018) for the Florida Keys WorldView image (68.3 and 65.1, respectively), and using our Chl_a value estimated from the same image. Kerr and Perkis (2018) reported that setting their Chl_a estimate for this image to 0.2 mg m^{-3} achieved the most accurate results. Our estimate for this image using equations 4–5 was 0.15 mg m^{-3}.

2.6. Implementation

We ran this algorithm on the 34 WV images with scripts written in Python and processed using a single core of the 1 Tesla K80 GPU running on a Dell C4130 server node at Oak Ridge National Laboratory. Images were run one at a time, but this method could be parallelized for future implementation. Advanced computational resources (e.g., high-performance computing clusters) were not necessary for implementing the algorithm, but could be leveraged for enhanced performance.

Output maps from each image were then mosaicked into a single bathymetry map in ArcMap. Overlap between scenes was handled by averaging coinciding pixels. As in Li et al. (2019), we did not correct the tidal effect of the WV-derived depth because the reference DTMs were collected over a period of three months at varying times of day and were not individually time-stamped.

2.7. Validation

Bathymetry was validated by calculating RMSE using the NOAA LiDAR-derived digital topobathymetric models (DTMs) as reference data (1-meter horizontal resolution). DTMs were created from LiDAR data acquired by aerial survey between November 2018 and March 2019. Bathymetry DTM vertical accuracy is reported at 11 cm (*NOAA Hurricane Irma, Florida Keys: Supplemental LiDAR & Shoreline Mapping*, 2020).

Validation points were created in ArcMap using the Create Random

Points tool by digitizing a bounding box for the study area and casting points within it that were separated from each other by at least 10 m to avoid spatial autocorrelation. Quality control included eliminating points that intersected cloud cover by digitizing clouds and removing intersected points. Additionally, DTMs featured data gaps surrounded by sparse, pixelated bathymetry data, which we assumed to correspond to poor LiDAR returns. We eliminated points that intersected data gaps and data-sparse regions. Bathymetry values were extracted for each point from our map and the DTM. Points that intersected land or contained No Data from either dataset were omitted from validation. A total of 635,081 validation points were used for estimating the accuracy of the resulting bathymetry map (Fig. 3).

3. Results

3.1. Processing time

Image processing was completed for all 34 images in 27 min, for an average processing time from ingestion of Level-1B images to output of mapped bathymetry of 47 s. This equated to mapping 138 km^2 per minute for this study area.

3.2. Bathymetry

3.2.1. Algorithm validation
RMSE was calculated for the entire map using all 635,081 validation points, as well as for 2-meter depth increments (Table 2). The overall RMSE was 1.95 m (0–15 m depth), and shallow depths saw consistent decreased error down to the 0–2 m increment with an RMSE of 1.16 m.

3.2.2. Spatial patterns
Bathymetry maps from this study and previous LiDAR DEM

Table 2
RMSE and sample size per depth range.

Depth (m)	RMSE (m)	n
<15	1.95	635,081
<12	1.90	629,169
<10	1.85	620,387
<8	1.73	583,292
<6	1.52	500,988
<4	1.28	397,549
<2	1.16	173,431

collections are displayed in Fig. 4. Our SDB map contains spatial patterns consistent with the DEM from the shallow Florida Bay region north of the Keys to areas > 15 m. Artifacts, however, are noticeable where images overlap. The averaging of overlapping pixels resulted in smoother transitions than simply using one image's pixel values, but imperfections in preprocessing, atmospheric correction, air-water interface correction, and water column correction are likely to create unavoidable artifacts. Additionally, inconsistencies may be expected where overlapping images were collected at substantially different times (e.g. over several years) and bathymetry changed.

4. Discussion

This study derives and implements a fully automated algorithm for mapping coastal bathymetry from 2-meter resolution satellite imagery without ground calibration data. The resulting wall-to-wall maps provide accurate bathymetry down to 15 m depth, and account for atmospheric attenuation, turbidity, and sun glint. We build on recent advances in the estimation of Chl-a concentration from optical imagery to account for inherent optical properties by refining algorithms to automate the identification of optically deep water. Through this
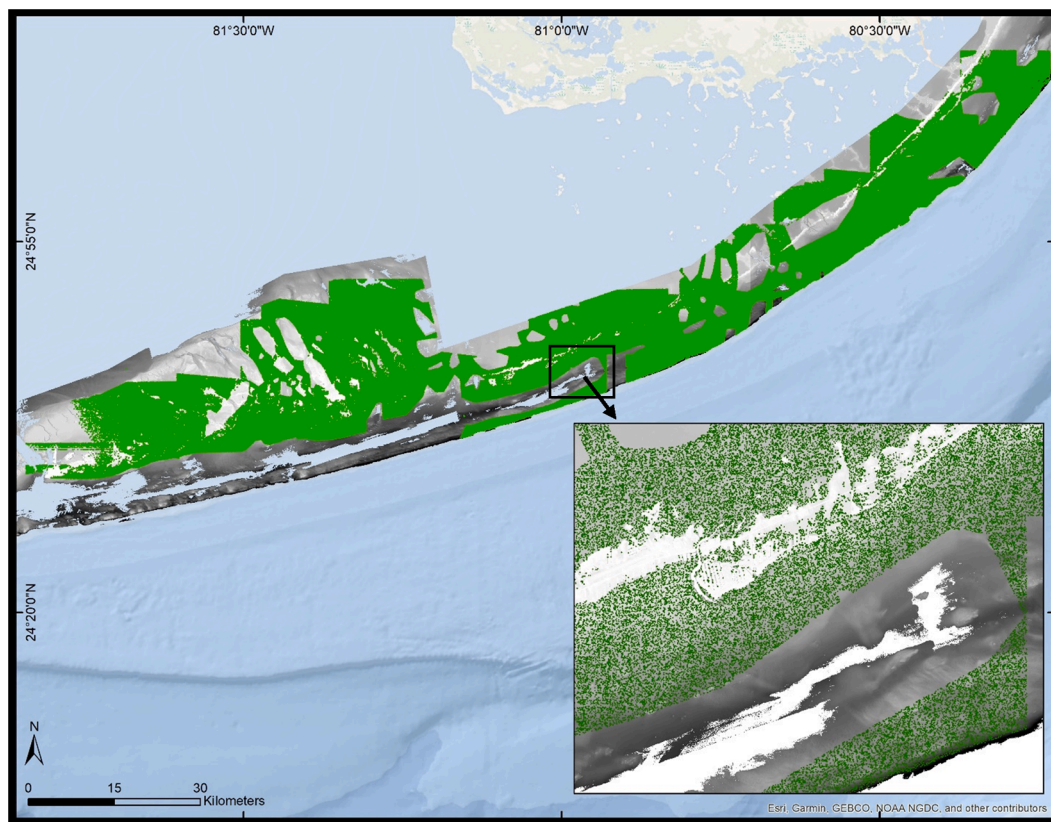

Fig. 3. Points used to evaluate map accuracy were created randomly throughout the map and separated from each other by 10 m. Inset shows land (i.e., positive elevation) and gaps in the validation DEM as white space that were excluded from validation.
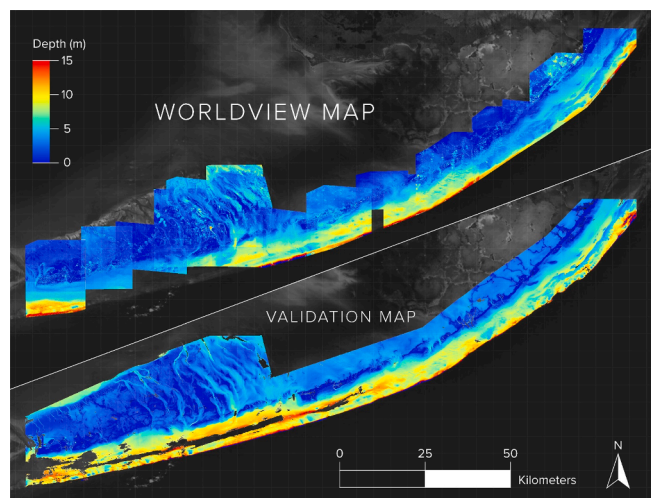
Fig. 4. Our WorldView-based map compared with the DEM validation map. Inset highlights bathymetric features along Key West.

refinement one is able to calculate used in the robust band ratio method (Stumpf et al., 2003).

Recent efforts to advance large-scale SDB mapping successfully developed IOP-estimation algorithms and demonstrated accurate derivation of tuning coefficients, but relied on single scenes for a given area (Kerr and Purkis, 2018; Zhu et al., 2020), or those manually selected for pristine viewing conditions that were then mosaicked during pre-processing to ensure consistent radiometry (Li et al., 2019). Our approach accounts for turbid water (assuming Chl-a-dominated turbidity), automatically identifies and corrects for any apparent sun glint, and applies robust radiometric calibration and atmospheric correction. These advances are significant in that they are more widely applicable to a variety of scene conditions (i.e., glinted or glint-free, moderately turbid or clear, collected across multiple years and all seasons), and require no manual preprocessing. As a result, this algorithm completed mapping from ingestion of Level-1B imagery to bathymetry-map output in less than one minute per image. Accuracy based on RMSE was 1.95 m, compared with 0.89–2.62 m (Kerr and Purkis, 2018),

1.22–1.86 m (Li et al., 2019), and 3.829 m (Zhu et al., 2020). Further, Fig. 5 demonstrates the consistent estimation of bathymetry patterns between our map and the validation data from shallow (i.e., <2 m) to deep (15 m) water along a 15 km transect in the middle of the study area. Two areas of erroneously shallow values appear to be caused by a sediment plume from the adjacent channel (center of plot), and a signal-to-noise weakness of the sensor to accurately detect deeper depths (right side of plot) as noted by Kerr and Perkis (Kerr and Purkis, 2018). Future work will include correcting for tides, which was not done here because the maps produced were validated against DTMs that were not tidally corrected.

Data availability statement

WorldView satellite imagery are commercial and are not available for public dissemination but may be ordered through the provider, DigitalGlobe. Validation DTMs may be downloaded through the NOAA DigitalCoast portal (https://coast.noaa.gov/digitalcoast/tools/dav.html).

CRediT authorship contribution statement

Matthew J. McCarthy: Conceptualization, Methodology, Software, Validation, Formal analysis, Writing – original draft. **Daniel B. Otis:** Conceptualization, Methodology, Validation. **David Hughes:** Conceptualization, Resources, Supervision, Writing – review & editing, Project administration. **Frank E. Muller-Karger:** Conceptualization, Resources, Supervision, Writing – review & editing, Funding acquisition, Project administration.
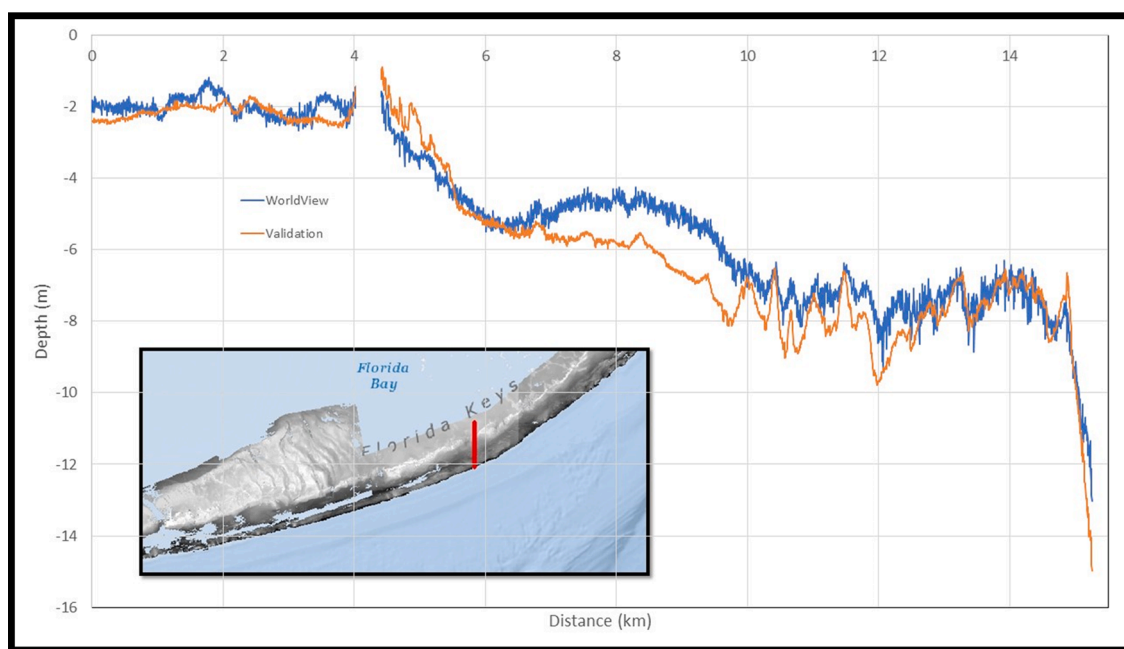

Fig. 5. Depth along a transect: WorldView map versus DEM validation map. The gap in values corresponds to land.

Declaration of Competing Interest

The authors declare that they have no known competing financial interests or personal relationships that could have appeared to influence the work reported in this paper.

Acknowledgements

References

Caballero, I., Stumpf, R.P., 2020. Atmospheric correction for satellite-derived bathymetry in the Caribbean waters: from a single image to multi-temporal approaches using Sentinel-2A/B. Opt. Express 28 (8), 11742. https://doi.org/10.1364/OE.390316.

Dash, P., Walker, N., Mishra, D., D'Sa, E., Ladner, S., 2012. Atmospheric correction and vicarious calibration of oceansat-1 Ocean Color Monitor (OCM) data in coastal case 2 waters. Remote Sensing 4, 1716–1740. https://doi.org/10.3390/rs4061716.

Hedley, J.D., Harborne, A.R., Mumby, P.J., 2005. Technical note: simple and robust removal of sun glint for mapping shallow-water benthos. Int. J. Remote Sens. 26 (10), 2107–2112. https://doi.org/10.1080/01431160500034086.

Hochberg, E.J., Andrefouet, S., Tyler, M.R., 2003. Sea surface correction of high spatial resolution ikonos images to improve bottom mapping in near-shore environments. IEEE Trans. Geosci. Remote Sensing 41 (7), 1724–1729. https://doi.org/10.1109/TGRS.2003.815408.

Hu, C., Lee, Z., Franz, B., 2012. Chlorophyll *a* algorithms for oligotrophic oceans: a novel approach based on three-band reflectance difference: a novel ocean chlorophyll A algorithm. J. Geophys. Res. 117 (C1) https://doi.org/10.1029/2011JC007395.

Hughes, D., Holyer, R., Lee, Z., 2001. Remote sensing algorithms by numerical inversion of radiative transfer models: neural network and optimization methods compared. In: Presented at the International Conference on Current Problems in Optics of Natural Waters, D.S. Rozhdestvensky Optical Society, St. Petersburg, Russia.

Jackson, C.R., Alpers, W., 2010. The role of the critical angle in brightness reversals on sunglint images of the sea surface. J. Geophys. Res. 115 (C9) https://doi.org/10.1029/2009JC006037.

Kay, S., Hedley, J., Lavender, S., 2009. Sun glint correction of high and low spatial resolution images of aquatic scenes: a review of methods for visible and near-infrared wavelengths. Remote Sensing 1, 697–730. https://doi.org/10.3390/rs1040697.

Kerr, J.M., Purkis, S., 2018. An algorithm for optically-deriving water depth from multispectral imagery in coral reef landscapes in the absence of ground-truth data. Remote Sens. Environ. 210, 307–324. https://doi.org/10.1016/j.rse.2018.03.024.

Kutser, T., Hedley, J., Giardino, C., Roelfsema, C., Brando, V.E., 2020. Remote sensing of shallow waters – a 50 year retrospective and future directions. Remote Sens. Environ. 240, 111619 https://doi.org/10.1016/j.rse.2019.111619.

Li, J., Knapp, D.E., Schill, S.R., Roelfsema, C., Phinn, S., Silman, M., Mascaro, J., Asner, G.P., 2019. Adaptive bathymetry estimation for shallow coastal waters using Planet Dove satellites. Remote Sens. Environ. 232, 111302. https://doi.org/10.1016/j.rse.2019.111302.

Li, J., Knapp, D.E., Lyons, M., Roelfsema, C., Phinn, S., Schill, S.R., Asner, G.P., 2021. Automated global shallow water bathymetry mapping using google earth engine. Remote Sensing 13, 1469. https://doi.org/10.3390/rs13081469.

Ma, Y., Zhang, H., Li, X., Wang, J., Cao, W., Li, D., Lou, X., Fan, K., 2021. An exponential algorithm for bottom reflectance retrieval in clear optically shallow waters from multispectral imagery without ground data. Remote Sensing 13, 1169. https://doi.org/10.3390/rs13061169.

Martin, J., Eugenio, F., Marcello, J., Medina, A., 2016. Automatic sun glint removal of multispectral high-resolution worldview-2 imagery for retrieving coastal shallow water parameters. Remote Sensing 8, 37. https://doi.org/10.3390/rs8010037.

Mayer, L., Jakobsson, M., Allen, G., Dorschel, B., Falconer, R., Ferrini, V., Lamarche, G., Snaith, H., Weatherall, P., 2018. The nippon foundation—GEBCO seabed 2030 project: the quest to see the world's oceans completely mapped by 2030. Geosciences 8, 63. https://doi.org/10.3390/geosciences8020063.

McCarthy, M.J., Radabaugh, K.R., Moyer, R.P., Muller-Karger, F.E., 2018. Enabling efficient, large-scale high-spatial resolution wetland mapping using satellites. Remote Sens. Environ. 208, 189–201.

McCarthy, M.J., Jessen, B., Barry, M.J., Figueroa, M., McIntosh, J., Murray, T., Schmid, J., Muller-Karger, F.E., 2020. Automated high-resolution time series mapping of mangrove forests damaged by hurricane Irma in Southwest Florida. Remote Sensing 12, 1740. https://doi.org/10.3390/rs12111740.

NOAA Hurricane Irma, Florida Keys: Supplemental LiDAR & Shoreline Mapping (Technical Data Report No. FL-1806-TB-C), 2020. Quantum Spatial, Corvallis, OR.

Overstreet, B.T., Legleiter, C.J., 2017. Removing sun glint from optical remote sensing images of shallow rivers: removing sun glint from river imagery. Earth Surf. Process. Landforms 42 (2), 318–333. https://doi.org/10.1002/esp.4063.

Sandidge, J.C., Holyer, R.J., 1998. Coastal bathymetry from hyperspectral observations of water radiance. Remote Sens. Environ. 65 (3), 341–352. https://doi.org/10.1016/S0034-4257(98)00043-1.

Shelestov, A., Lavreniuk, M., Kussul, N., Novikov, A., Skakun, S., 2017. Exploring google earth engine platform for big data processing: classification of multi-temporal satellite imagery for crop mapping. Front. Earth Sci. 5 https://doi.org/10.3389/feart.2017.00017.

Stocker, T.F., Qin, D., Plattner, G.-K., Tignor, M., Allen, S.K., Boschung, J., Nauels, A., Xia, Y., Bex, V., Midgley, P.M., 2013. Climate Change 2013: The Physical Science Basis. Cambridge University Press, Cambridge, UK.

Stumpf, R.P., Holderied, K., Sinclair, M., 2003. Determination of water depth with high-resolution satellite imagery over variable bottom types. Limnol. Oceanogr. 48 (1part2), 547–556. https://doi.org/10.4319/lo.2003.48.1_part_2.0547.

Werdell, P.J., Bailey, S.W., 2005. An improved in-situ bio-optical data set for ocean color algorithm development and satellite data product validation. Remote Sens. Environ. 98 (1), 122–140. https://doi.org/10.1016/j.rse.2005.07.001.

Zhou, G., Xu, W., Niu, C., Zhang, K., Ma, Z., Wang, J., Zhang, Y., 2017. Versatile time-dependent spatial distribution model of sun glint for satellite-based ocean imaging. J. Appl. Remote Sens 11 (1), 016020. https://doi.org/10.1117/1.JRS.11.016020.

Zhu, J., Hu, P., Zhao, L., Gao, L., Qi, J., Zhang, Y., Wang, R., 2020. Determine the stumpf 2003 model parameters for multispectral remote sensing shallow water bathymetry. J. Coastal Res. 102 https://doi.org/10.2112/SI102-007.1.